Strongly interacting bosons on a three-leg ladder in the presence of a homogeneous flux

You may also be interested in:

Ground states of a Bose–Hubbard ladder in an artificial magnetic field: field-theoretical approach
Akiyuki Tokuno and Antoine Georges

Incommensurate phases of a bosonic two-leg ladder under a flux
E Orignac, R Citro, M Di Dio et al.

Methods for detecting charge fractionalization and winding numbers in an interacting fermionic ladder
Leonardo Mazza, Monika Aidelsburger, Hong-Hao Tu et al.

Light-induced gauge fields for ultracold atoms
N Goldman, G Juzelinas, P Öhberg et al.

Synthetic gauge fields in synthetic dimensions: interactions and chiral edge modes
Simone Barbarino, Luca Taddia, Davide Rossini et al.

Density-induced geometric frustration of ultra-cold bosons in optical lattices
T Mishra, S Greschner and L Santos

Quantum spin nanotubes—frustration, competing orders and criticalities
Tôru Sakai, Masahiro Sato, Kiyomi Okamoto et al.

FAST TRACK COMMUNICATION

Strongly interacting bosons on a three-leg ladder in the presence of a homogeneous flux

F Kolley[1], M Piraud[1], I P McCulloch[2], U Schollwöck[1] and F Heidrich-Meisner[1]

[1] Department of Physics and Arnold Sommerfeld Center for Theoretical Physics, Ludwig-Maximilians-Universität München, D-80333 München, Germany
[2] ARC Centre for Engineered Quantum Systems, School of Mathematics and Physics, The University of Queensland, St Lucia, Queensland 4072, Australia

E-mail: marie.piraud@physik.uni-muenchen.de

Abstract

We perform a density-matrix renormalization-group study of strongly interacting bosons on a three-leg ladder in the presence of a homogeneous flux. Focusing on one-third filling, we explore the phase diagram in dependence of the magnetic flux and the inter-leg tunneling strength. We find several phases including a Meissner phase, vortex liquids, a vortex lattice, as well as a staggered-current (SC) phase. Moreover, there are regions where the chiral current reverses its direction, both in the Meissner and in the SC phase. While the reversal in the latter case can be ascribed to spontaneous breaking of translational invariance, in the first it stems from an effective flux increase in the rung direction. Interactions are a necessary ingredient to realize either type of chiral-current reversal.

1. Introduction

Experimental progress with ultracold quantum gases has made feasible engineering the coupling between the different states of the atoms, in order to realize synthetic gauge fields [1, 2]. The effective magnetic fields acting on the neutral atoms can be much larger than what is possible in solid-state systems. These advances bring the simulation of a wide range of Hamiltonians into reach that are important in condensed matter physics [3–8]. Indeed, some of the most intriguing phenomena in condensed matter physics involve the presence of strong magnetic fields. For instance, topological states of matter are realized in quantum Hall systems [9, 10], which are insulating in the bulk, but bear conducting edge states. Remarkably, topological phase transitions were observed in experiments with cold atoms [11–13].

Recently, there has been a growing theoretical (see, e.g., work on fermions [14–16] and bosons [17–23]) and experimental [24–26] interest in quasi-one dimensional relatives of the square lattice [27–37], the *N*-leg ladder systems with synthetic gauge fields. Besides using superlattices [24] to realize these geometries, a synthetic lattice dimension can be exploited where the sites on the rungs of the ladder correspond to different hyperfine states [38]. The latter has motivated several recent theoretical studies [39–44]. Chiral edge currents on two- and three-leg ladders subjected to a homogeneous flux have been observed using both experimental approaches, for bosons [24, 26] and fermions [25]. The physics of interacting bosons on ladders has also been studied in the context of Josephson junction arrays [45–48], albeit in the weakly-interacting regime.

Such *N*-leg ladder systems, similar to their counterparts in quantum magnetism [49], provide an elegant bridge between the physics in one and two dimensions [50]. Interacting bosons on two-leg ladders in homogeneous magnetic fields harbor very rich physics, featuring Meissner and vortex phases [17–19, 21, 23, 51–53], a biased-ladder phase that breaks the symmetry between the two legs [22, 54, 55], analogues of Laughlin states [56] as well as an interaction-driven reversal of the direction of the current due to spontaneous breaking of translational invariance in vortex lattices (VLs) [22].
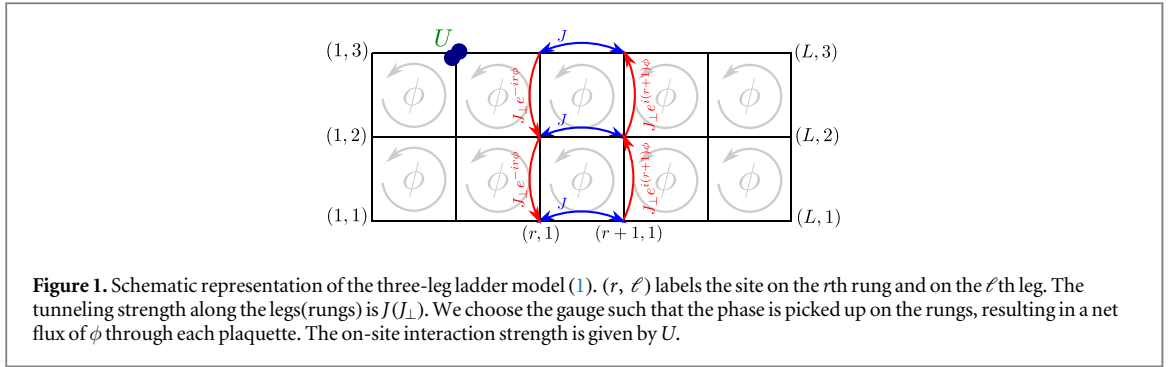
Figure 1. Schematic representation of the three-leg ladder model (1). (r, ℓ) labels the site on the rth rung and on the ℓth leg. The tunneling strength along the legs(rungs) is $J (J_\perp)$. We choose the gauge such that the phase is picked up on the rungs, resulting in a net flux of ϕ through each plaquette. The on-site interaction strength is given by U.

Here, we use density-matrix renormalization-group (DMRG) [57–59] simulations to explore the phase diagram of strongly interacting bosons on a three-leg ladder subjected to a homogeneous flux. We focus on a filling of one-third of a boson per site, which can easily be realized in experiments [26]. At this filling, the system is expected to be in a Mott-insulating state, based on the existence of a magnetization plateau at one-third of the saturation magnetization in the closely related three-leg spin-1/2 ladders [60, 61] and on work on the MI-SF transition in bosomic three-ladders at zero flux a zero flux [74]. We present the phase diagram for hard-core bosons (HCBs) in dependence of the inter-leg coupling strength and the magnitude of the magnetic flux. As a main result, we observe vortex phases that cannot be traced back to features in the single-particle dispersion. In the Meissner phase in this system, there is a fascinating reversal of the direction of the current, driven by the magnetic flux. We provide an explanation for this effect and we show that it persists at intermediate interaction strengths. Finally, a staggered-current (SC) phase, generalizing the one found on the two-leg ladder [17, 18], is observed around $\phi \sim \pi$, which also triggers a chiral-current reversal.

2. Model and method

We consider the Bose-Hubbard Hamiltonian on a three-leg ladder of length L (see figure 1):

$$
\mathcal{H} = -J_\perp \sum_{r=1}^{L}\sum_{\ell=1}^{2} \left(e^{-ir\phi} a_{r,\ell}^\dagger a_{r,\ell+1} + \text{h. c.} \right)
$$
$$
- J \sum_{r=1}^{L-1}\sum_{\ell=1}^{3} \left(a_{r,\ell}^\dagger a_{r+1,\ell} + \text{h. c.} \right) + \frac{U}{2} \sum_{r=1}^{L}\sum_{\ell=1}^{3} n_{r,\ell} \left(n_{r,\ell} - 1 \right), \tag{1}
$$

where $a_{r,\ell}^\dagger$ creates a boson on the rth rung and the ℓth leg of the system and $n_{r,\ell} \equiv a_{r,\ell}^\dagger a_{r,\ell}$ is the on-site number operator. J and $J_\perp$ are the tunneling matrix elements along the legs and rungs, respectively, U is the on-site interaction strength, and ϕ is the magnetic flux through a plaquette of the ladder.

We compute the ground state of (1) numerically with a single-site DMRG algorithm [62]. While exploiting the $U(1)$ symmetry of the Hamiltonian associated to particle number conservation, we keep up to 4000 DMRG states and the data in the figures of the main text are for $L = 100$, while we have considered L as large as $L = 200$ in the appendix. For $U/J < \infty$, we limit the number of bosons per site to six at maximum. For the determination of the Mott insulator (MI) to superfluid (SF) transitions, we use infinite-size DMRG [63] with up to 600 DMRG states (see appendix B).

The different phases are primarily characterized by their local current configurations. The associated operators are

$$
j_{r,\ell}^\parallel = iJ \left(a_{r+1,\ell}^\dagger a_{r,\ell} - a_{r,\ell}^\dagger a_{r+1,\ell} \right), \tag{2}
$$

$$
j_{r,\ell}^\perp = iJ_\perp \left(e^{-ir\phi} a_{r,\ell+1}^\dagger a_{r,\ell} - e^{ir\phi} a_{r,\ell}^\dagger a_{r,\ell+1} \right). \tag{3}
$$

We compute the chiral current from

$$
j_{\text{C}} = \frac{1}{2L} \sum_r \langle j_{r,1}^\parallel - j_{r,3}^\parallel \rangle. \tag{4}
$$

Throughout the paper, we fix the filling to 1/3 bosons per site.

Figure 2. Phase diagram for HCBs with $1/3$ particle per site on average, as a function of $J_\perp$ and ϕ. The dotted lines are upper bounds for the Mott-insulator (MI) to superfluid (SF) transition, as determined by an analysis of the Binder cumulant corresponding to an appropriate string-order parameter (see appendix B). The phase diagram features Meissner (M-MI/M-SF), vortex-liquid (V), vortex-lattice (VL) and staggered-current (SC-MI/SC-SF) phases. While the SC region is split into a Mott insulating and a superfluid phase, the V and VL phases are Mott insulating, in the Meissner phase, the color encodes the amplitude of the chiral current j_C. The gray '+' symbols mark the parameter points analyzed with DMRG. Large black diamonds denote the parameter values for which the local-current patterns are presented in figure 3. The vortex-liquid region contains one- and two-component Luttinger liquids. The VL is expected to be surrounded by a (possibly very thin) vortex-liquid phase.

3. Phase diagram

### 3.1. Summary of results for two-leg ladders

Let us first briefly summarize some results for the corresponding two-leg ladder model in the low density regime (obtained by limiting the number of legs to two in figure 1), which will help to appreciate our results for the three-leg ladder to be presented in the following. The phase diagram for HCBs at a filling of one boson per rung has been reported in [21, 23]: at fixed rung coupling $J_\perp/J < 1.6$, there is a transition from a phase with Meissner-like currents to a vortex phase when increasing the flux. Above a critical value $J_\perp^c \simeq 1.6J$, the Meissner phase is stable at any flux. Furthermore, at certain commensurate vortex densities, VLs are expected to form [51], which, however, do not seem to exist in the limit of HCBs [21]. At smaller interaction strength, though, stable VLs at vortex densities of $1/2$ and $1/3$ have been identified in [22]. In those phases, the translation invariance associated with translations along the legs of the ladder is spontaneously broken and an enlarged unit cell forms. As a consequence, the effective flux sensed by the bosons is modified. This leads to a spontaneous reversal of the direction of the chiral current, under certain conditions on the flux and interaction strength [22].

3.2. Overview of the phase diagram for the three-leg ladder

Figure 2 shows the ground-state phase diagram for HCBs [$(a_{r,\ell}^\dagger)^2 = 0; U/J \to \infty$] of the three-leg ladder model equation (1) as a function of $J_\perp \in [J, 2J]$ and flux. Results are displayed for $\phi \in [0, \pi]$ since all physical quantities are 2π-periodic, odd or even, functions of the flux [22]. We find the following phases: (i) a Meissner phase (M-MI/M-SF), which shows a reversal of the current direction for large values of the flux, (ii) vortex-liquid phases (V), (iii) a VL phase, and (iv) SC phases (SC-MI/SC-SF). The corresponding transitions are located by solid lines in figure 2, in which the gray '+' symbols indicate the parameter points that were analyzed numerically. For $J_\perp/J \gtrsim 1.6$ or $\phi \gtrsim 0.3\pi$, we observe a finite mass gap (see appendix B) indicating that the system is in a Mott-insulating state. This is inherited from the $J_\perp/J \gg 1$ limit, in which the ground state is the product of the local ground state on each rung, separated by a gap $\sqrt{2}J_\perp$ from all excited states (similar to the two-leg ladder with one boson per rung [64]). Upon lowering $J_\perp$ at fixed ϕ, the mass gap eventually closes. The computation of the Binder cumulant [65] of an appropriate string-order parameter for the Mott insulator yields an upper bound for the transition to a SF phase when lowering $J_\perp$ (see the dotted line in figure 2). This transition is, for $\phi/\pi \lesssim 0.3$, compatible with a Berezinskii–Kosterlitz–Thouless transition (see appendix B) as expected from the theoretical work on magnetization plateaux in N-leg spin ladders [60, 61] and numerical work at $\phi = 0$ [74]. The transition at $0.9 < \phi/\pi \leqslant 1$, on the other hand, is compatible with a second-order phase transition (see appendix B). In the following, we refer to states with a Meissner-like current configurations using the label M, and to states with a SC pattern using the label SC (irrespective of whether these are MI or SF phases).
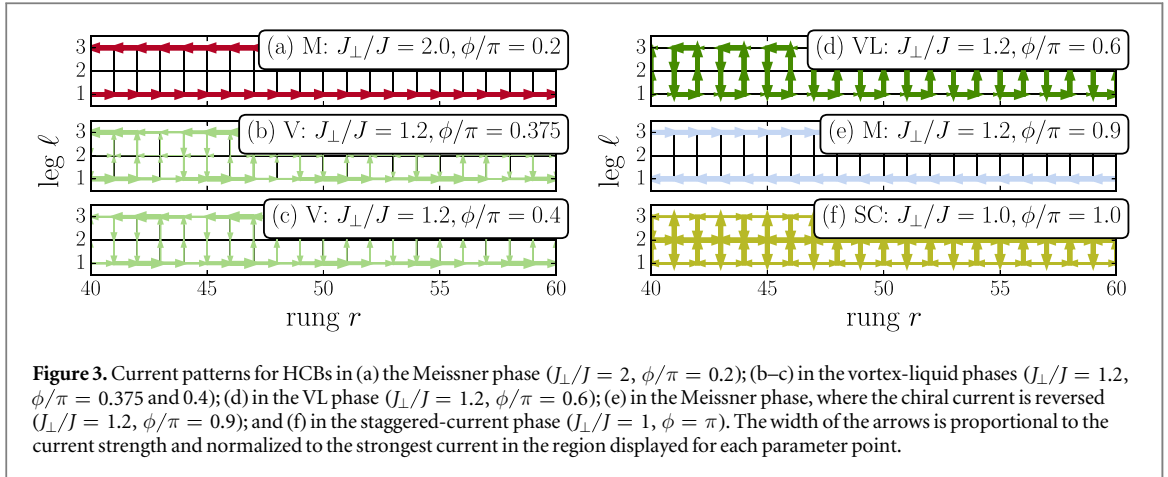
Figure 3. Current patterns for HCBs in (a) the Meissner phase ($J_\perp/J = 2$, $\phi/\pi = 0.2$); (b–c) in the vortex-liquid phases ($J_\perp/J = 1.2$, $\phi/\pi = 0.375$ and 0.4); (d) in the VL phase ($J_\perp/J = 1.2$, $\phi/\pi = 0.6$); (e) in the Meissner phase, where the chiral current is reversed ($J_\perp/J = 1.2$, $\phi/\pi = 0.9$); and (f) in the staggered-current phase ($J_\perp/J = 1$, $\phi = \pi$). The width of the arrows is proportional to the current strength and normalized to the strongest current in the region displayed for each parameter point.
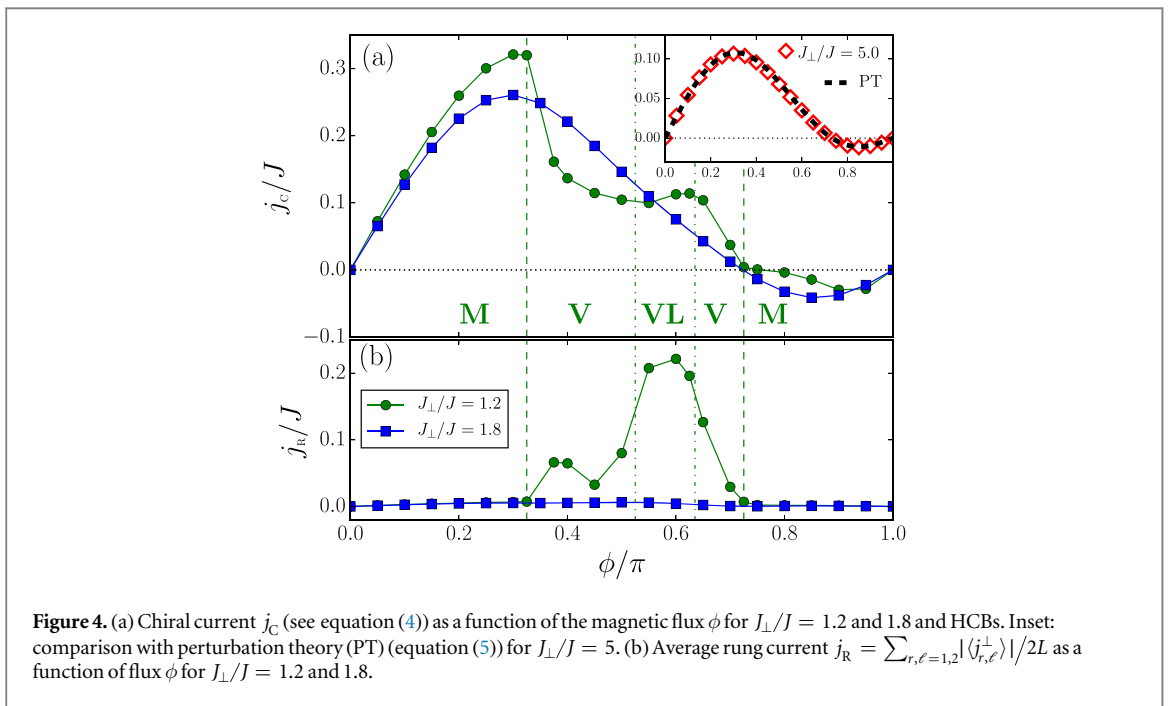

Figure 4. (a) Chiral current j_C (see equation (4)) as a function of the magnetic flux ϕ for $J_\perp/J = 1.2$ and 1.8 and HCBs. Inset: comparison with perturbation theory (PT) (equation (5)) for $J_\perp/J = 5$. (b) Average rung current $j_R = \sum_{r,\ell=1,2} |\langle j_{r,\ell}^\perp \rangle|/2L$ as a function of flux ϕ for $J_\perp/J = 1.2$ and 1.8.

3.3. Meissner phases

For $J_\perp/J \geqslant 1.6$, only a Meissner phase exists, characterized by currents occurring exclusively in the upper and the lower leg (see figures 3(a) and (e)), with a finite mass gap. The existence of such a Meissner-Mott insulator (M-MI) on the three-leg ladder has been predicted in reference [56]. For $\phi/\pi \lesssim 0.3$, we find a transition from this Mott-insulator to a SF phase with Meissner currents (M-SF) by lowering the inter-chain coupling $J_\perp$ (dashed line in figure 2). Intriguingly, the chiral current reverses its chirality from counterclockwise (figure 3(a)) to clockwise (figure 3(e)) for $\phi/\pi \gtrsim 0.75$, meaning that the atoms flow in the direction opposite to the one favored by the effective magnetic field. As a consequence, at the point at which the reversal occurs, no current flows even though the bosons feel a very strong, non-staggered, magnetic flux. A typical example for the $j_C = j_C(\phi)$ curve in the Meissner phase is shown in figure 4(a) for $J_\perp/J = 1.8$. The curve is smooth as there is no phase transition.

3.4. Vortex phases

Upon lowering $J_\perp$ to $J_\perp/J \lesssim 1.5$, the Meissner phase is split by vortex phases at intermediate values of the flux. Typical current patterns in the vortex phases, which, for open boundary conditions, exhibit non-zero rung currents $\langle j_{r,\ell}^\perp \rangle$, are presented in figures 3(b)–(d). We also plot the chiral current j_C (see figure 4(a)) as a function of ϕ for $J_\perp/J = 1.2$, together with the average absolute value of the rung current $j_R = \sum_{r,\ell=1,2} |\langle j_{r,\ell}^\perp \rangle|/2L$ (see figure 4(b)). The transition from the Meissner into the vortex phases is characterized by j_R becoming non-zero and by kinks in the $j_C = j_C(\phi)$ curves (see the example of $J_\perp/J = 1.2$). The vortex phases can be further divided
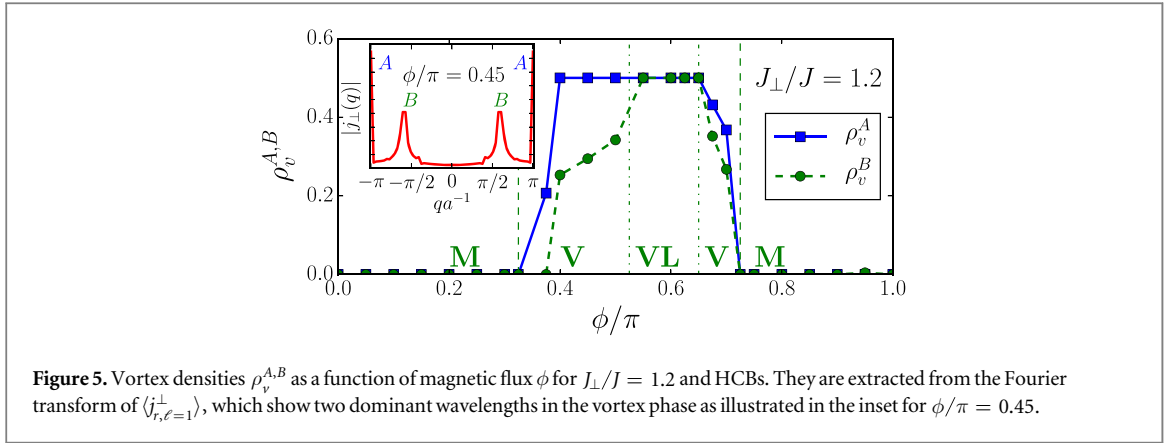
Figure 5. Vortex densities $\rho_v^{A,B}$ as a function of magnetic flux ϕ for $J_\perp/J = 1.2$ and HCBs. They are extracted from the Fourier transform of $\langle j_{r,\ell=1}^\perp \rangle$, which show two dominant wavelengths in the vortex phase as illustrated in the inset for $\phi/\pi = 0.45$.

into vortex-liquid (V) phases, which are incommensurate, gapless phases (see, e.g., figures 3(b)–(c)) and a VL, which is fully gapped and forms at a commensurate vortex density [51] (see, e.g., figure 3(d)).

3.4.1. Vortex lattice

The commensurability of the phases can be unveiled by studying the spatial patterns of the rung currents $\langle j_{r,\ell=1}^\perp \rangle$. In general, their Fourier transforms bear two typical wavelengths q_A and q_B (see the inset of figure 5, we choose $|q_B| < |q_A|$). Motivated by this observation, we define two vortex densities $\rho_v^{A,B} = q_{A,B} a^{-1}/(2\pi)$ (with a the lattice spacing), which are shown in figure 5 for $J_\perp/J = 1.2$. In the Meissner and VL phases, both vortex densities are commensurate with $\rho_v^\alpha = 0$ and $\rho_v^\alpha = 1/2$ (with $\alpha = A, B$), respectively. These two phases are fully gapped. In the case of the VL, we ascribe this behavior to the incompressibility of the vortex pattern: it costs a finite energy to add a vortex to the system, even in the thermodynamic limit. The transitions to the vortex-liquid phases are continuous commensurate-incommensurate transitions [51]. We therefore expect the vortex-liquid region to surround the VL phase everywhere, even though the proximity of various phase transitions renders it very difficult to resolve numerically.

3.4.2. Vortex liquids

The incommensurate vortex-liquid region (V) encompasses phases in which both vortex densities are incommensurate (e.g., at $\phi/\pi = 0.7$ in figure 5) as well as phases where one mode is commensurate (at either $\rho_v^\alpha = 0$ or $\rho_v^\alpha = 1/2$) and the other is not (e.g., at $\phi/\pi = 0.375$ and 0.5 in figure 5). This is fully corroborated by the study of the von Neumann entropy, yielding either a central charge $c = 2$ or $c = 1$ (see appendix A) in the vortex-liquid phases, corresponding to two- and one-component Luttinger liquids, respectively (we do not distinguish between the $c = 1$ and $c = 2$ vortex-liquid phase in the figures). In principle, the study of current-current correlations could also permit to distinguish the different vortex phases. However, the superposition of the behaviours of the different components renders the analysis of correlations less conclusive for finite-size systems.

We stress that the emergence of vortex phases for bosons on the three-leg ladder is a many-body effect: the minimum of the single-particle dispersion is always at zero momentum, corresponding to a Meissner phase with counterclockwise chiral-current. The vortex phases are thus not inherited from finite-momentum global minima in the single-particle dispersion relation, unlike in two-leg ladders [11, 21, 22, 52].

3.4.3. Staggered-current phase

Around $J_\perp \sim J$ and for $\phi \lesssim \pi$, a phase with SC emerges (see figure 3(f)). It is characterized by strong currents going around each plaquette. This phase breaks translation invariance along the legs of the ladder and has a commensurate vortex density $\rho_v^\alpha = 1/2$, corresponding to a spatial periodicity of two lattice sites. It can be visualized as two VL states on the upper and lower two-leg ladder, shifted by one site with respect to each other. This phase shows a Mott-insulator to SF transition when lowering $J_\perp/J$ (see figure 2 and appendix B). At $\phi = \pi$, the Hamiltonian (1) is real, and therefore, time-reversal invariant. The SC phases then spontaneously break this symmetry (see figure 3(f)): reversing all currents does not leave the pattern invariant; they can thus be viewed as a generalization of the chiral Mott-insulator and SF phases realized on two-leg ladders [17, 18].

3.5. Chiral-current reversal in the Meissner phase

Let us further investigate the region $\phi/\pi \gtrsim 0.75$ where the chirality of the chiral currents is opposed to the one favored by the bare flux. In the strong-rung limit $J_\perp \gg J$, the three-site problem is solved analytically and
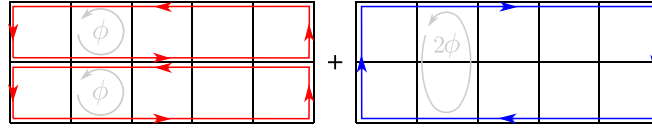
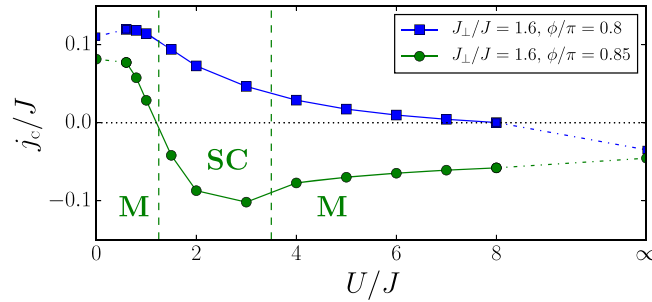**Figure 6.** Schematic representation of the two contributions to equation (5) for $\pi/2 < \phi < \pi$.

Figure 7. Chiral current j_C as a function of on-site interaction U for $J_\perp/J = 1.6$ and $\phi/\pi = 0.8$ and 0.85.

standard perturbation theory (PT) can be applied. To first order in $J/J_\perp$, the chiral current is then given by

$$j_C^{\text{PT}} = \frac{J^2}{2\sqrt{2}J_\perp}\left(\sin\phi + \frac{3}{4}\sin 2\phi\right), \tag{5}$$

which implies a reversal of the current at $\phi = \arccos(-2/3) \approx 0.73\pi$, independently of $J_\perp$. Equation (5) agrees very well with the DMRG calculations for $J_\perp/J = 5$ (see the inset of figure 4(a)), and the parameter point at which the reversal occurs barely moves for $J_\perp/J \gtrsim 1.6$ (see figure 2).

The flux dependence $j_C \propto \sin(\phi)$ is directly inherited from that of the two-leg ladder in the Meissner phase [21]. The two terms of (5) can therefore be interpreted as stemming from two contributions, which are sketched in figure 6. The first term (left panel) corresponds to chiral currents flowing on the two sub-ladders (formed by the middle leg and the upper or lower leg) resulting in a zero net-current on the middle leg, whereas the second term (right panel) corresponds to particles propagating only along the top and bottom leg of the three-leg ladder. This can be thought of as a Meissner phase with an effective flux $\phi_{\text{eff}} = 2\phi$. For $\pi/2 < \phi < \pi$, the second contribution is negative, which can lead to a total chiral current with a reversed chirality. This reversal is thus associated with a doubling of the effective flux along the rung direction. It can already be captured in the minimal model of two plaquettes $(L = 2)$, in which a qualitatively similar reversal occurs in the strongly interacting limit. An increase of the effective flux also underlies the chiral-current reversal in the case of two-leg ladders [22], yet there, the increase results from spontaneous breaking of translation symmetry.

The $J_\perp \gg J$ limit also permits to understand another numerical observation: the density is imbalanced between the legs, in all phases. PT indeed predicts a density twice as large on the middle leg than on the outer ones. This difference decreases when lowering $J_\perp/J$.

3.6. Finite interactions $U/J < \infty$

In the single-particle case $(U/J = 0)$, the Meissner phase has counterclockwise chirality for any choice of parameters. Therefore, there must be a reversal of the chiral current as the interaction strength increases. This is indeed the case as shown in figure 7, displaying j_C as a function of U, for $\phi/\pi = 0.8$ and 0.85 and $J_\perp/J = 1.6$. The reversal from a negative to a positive current occurs at a finite interaction strength U whose value depends on ϕ. For $\phi/\pi = 0.85$, the system enters into a SC phase at intermediate values of U, as indicated in the figure. Translational invariance is spontaneously broken in the SC phase and the unit cell comprises four plaquettes (see figure 3(f)). For $\phi \in [3\pi/4, \pi]$, the effective flux is $\phi_{\text{eff}} = 4\phi \in [-\pi, 0]$ modulo 2π, and the current is reversed. This realizes another instance of the chiral-current reversal due to spontaneously enlarged unit cells first presented in reference [22]. The presence of the SC phases stabilizes the current reversal down to much smaller values of U/J compared to parameters for which the SC phase is absent (compare the data for $\phi/\pi = 0.8$ and 0.85 shown in figure 7). Note that the VL phase leads to the same unit-cell enlargement. However, as it occurs for $\phi \in [\pi/2, 3\pi/4]$ in the HCBs case (see figure 2), one has $\phi_{\text{eff}} = 4\phi \in [0, \pi]$ modulo 2π, and the chiral current is not reversed.
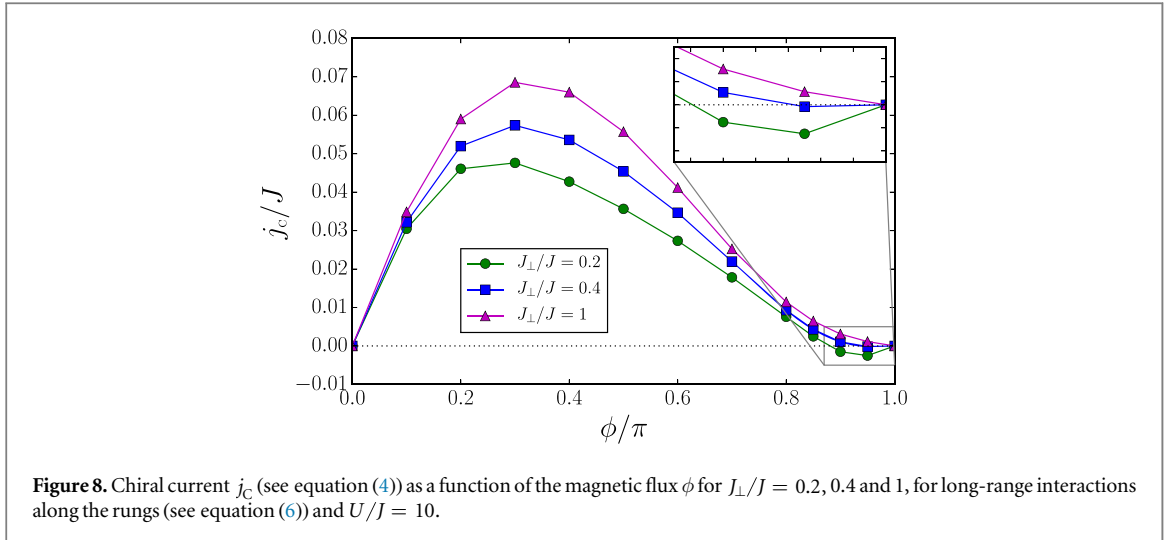
Figure 8. Chiral current j_C (see equation (4)) as a function of the magnetic flux ϕ for $J_\perp/J = 0.2$, 0.4 and 1, for long-range interactions along the rungs (see equation (6)) and $U/J = 10$.

4. Experimental realizations

The most straightforward experimental approach would be to use a superlattice to split a two-dimensional lattice into three-leg ladders [66]. This would create an energy offset between the middle and the outer two legs, which could easily be compensated by another superlattice with a two-site periodicity. For systems with a synthetic lattice dimension [25, 26, 38], the interaction in the rung direction is not on-site as considered here, but depends on the total density $n_r^t = \sum_{\ell=1}^{3} n_{r,\ell}$ in all three rung sites. Thus, the appropriate form is

$$H_{\text{int}} = \frac{U}{2}\sum_{r=1}^{L} n_r^t \left(n_r^t - 1\right).$$

(6)

Our DMRG results for $U/J = 10$ show that this type of long-range interactions suppresses vortex phases. This is qualitatively consistent with the study of the two-leg ladder, in which this type of interaction also favors the Meissner phase over the vortex phase [19, 56]. The chiral-current reversal in the Meissner phase at a filling of one-third survives at small $J_\perp/J \lesssim 0.3$ (see figure 8).
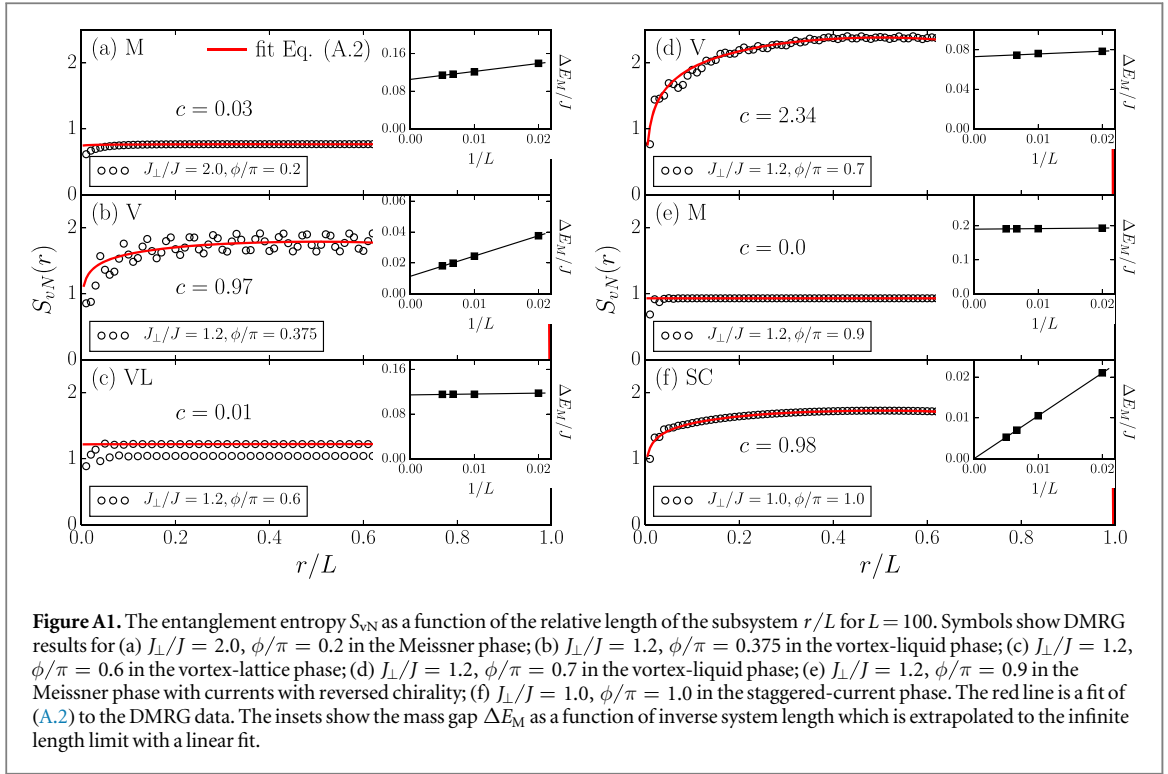
5. Summary

We presented the phase diagram of strongly-interacting bosons on a three-leg ladder subjected to a homogeneous magnetic flux. We identified several phases, including vortex-liquid phases, a vortex lattice and a Meissner phase. Moreover, there is a state with staggered currents, which leads to a reversal of the chiral current due to the spontaneous increase of the unit cell, similar to the situation discussed in [22]. Fascinatingly, the Meissner phase also shows a chiral-current reversal when increasing the strength of the magnetic flux per plaquette, yet in the Meissner phase, translational invariance is not broken. The analysis of the strong-rung and large-interaction limit indicates that a doubled flux is experienced along the rung direction. Therefore, the chiral-current reversal in the Meissner phase is qualitatively different. We argue that interactions are a necessary ingredient to obtain these behaviors.

Acknowledgments

Figure A1. The entanglement entropy S_{vN} as a function of the relative length of the subsystem r/L for $L = 100$. Symbols show DMRG results for (a) $J_\perp/J = 2.0$, $\phi/\pi = 0.2$ in the Meissner phase; (b) $J_\perp/J = 1.2$, $\phi/\pi = 0.375$ in the vortex-liquid phase; (c) $J_\perp/J = 1.2$, $\phi/\pi = 0.6$ in the vortex-lattice phase; (d) $J_\perp/J = 1.2$, $\phi/\pi = 0.7$ in the vortex-liquid phase; (e) $J_\perp/J = 1.2$, $\phi/\pi = 0.9$ in the Meissner phase with currents with reversed chirality; (f) $J_\perp/J = 1.0$, $\phi/\pi = 1.0$ in the staggered-current phase. The red line is a fit of (A.2) to the DMRG data. The insets show the mass gap ΔE_M as a function of inverse system length which is extrapolated to the infinite length limit with a linear fit.

Appendix A. Entanglement entropy

The entanglement entropy S_{vN} is defined as the von Neumann entropy corresponding to a bipartition of the wavefunction into two subsystems A and B:

$$S_{vN} = -\mathrm{Tr}\,\rho_A \ln \rho_A, \tag{A.1}$$

where $\rho_A = \mathrm{Tr}_B |\psi\rangle\langle\psi|$ is the reduced density matrix of subsystem A. In conformal field theory, for a one-dimensional system with open boundary conditions and total length L, the von Neumann entropy of a subsystem of length r is given by [67, 68]

$$S_{vN}(r) = \frac{c}{6}\log\left[\frac{2L}{\pi}\sin\left(\frac{\pi r}{L}\right)\right] + g, \tag{A.2}$$

where c is the central charge of the conformal field theory and g is a non-universal constant. The central charge measures the number of gapless modes in the system.

In figure A1 we show the entanglement entropy $S_{vN}(r)$ for straight cuts through the three-leg ladder between rungs r and $r + 1$. By fitting (A.2) to the data we obtain estimates for the central charge. Oscillations of the entropy in the vortex phases make the fit very sensitive to the fitting region used. This applies, in particular, to the vortex-liquid phases. Nevertheless, the behavior of the central charge provides further insights into the nature of the commensurate-incommensurate transition.

In the Meissner phase (figures A1(a) and (e)) the values of the central charge are very close to zero in agreement with an entanglement entropy independent of the subsystem size, which corresponds to the area law of a fully gapped phase [69].

The vortex phases can be divided into vortex-liquid and VL phases with incommensurate and commensurate vortex densities, respectively. As illustrated in figure 5 of the main text there are two vortex densities that undergo a transition from the Meissner to a vortex-liquid and VL phase with increasing flux ϕ/π and at low enough $J_\perp/J$. This picture is consistent with the behavior of the central charge. More precisely, at $J_\perp/J = 1.2$ and $\phi/\pi = 0.375$, we find one incommensurate vortex density in the Fourier transform of the rung currents and a central charge of $c \approx 1$ (figure A1(b)). At flux $\phi/\pi = 0.7$, there are two incommensurate vortex densities. The central charge is $c \approx 2$ in agreement with the presence of two gapless modes (figure A1(d)). At $\phi/\pi = 0.6$, both vortex densities are commensurate and we find an entanglement entropy independent of subsystem size (up to oscillations due to the increased unit cell), or $c = 0$ in terms of the central charge (figure A1(c)).

This suggests that the modes, which are measured by the central charge, can be related to the dominating vortex densities in the Fourier transform of the rung currents. An incommensurate vortex density would be associated with a gapless mode while a commensurate vortex density would correspond to a gapped mode.

In the SC phase the vortex densities are commensurate, while the fit gives a central charge $c \approx 1$. But the scaling of the entanglement spectrum indicates that it is two independent $c=0.5$ modes, and also the scaling of the correlation function gives the scaling dimension $\Delta \simeq 1/8$ (not shown), consistent with $c=0.5$. This indicates that the mass gap is closed, which is compatible with the analysis of the mass gap and the Binder cumulant presented in the next section.

Appendix B. Mott insulator to superfluid transition

The mass gap ΔE_M is defined as

$$\Delta E_M = \frac{1}{2}[E(N-1) + E(N+1)] - E(N), \tag{B.1}$$

where $E(N)$ is the total ground-state energy of the system with N particles.

We generally observe a finite mass gap that becomes smaller when decreasing the inter-leg coupling $J_\perp$. In the $J_\perp = 0$ limit, the mass gap is known to be closed. As already mentioned in the main text, in the $\phi/\pi = 0$ limit, the transition to the SF phase at finite $J_\perp/J$ can be expected to be of the Berezinskii–Kosterlitz–Thouless type [60, 61], and, therefore, is very hard to pinpoint numerically.

In the insets of figure A1 we show the mass gap as a function of the inverse system size $1/L$ extrapolated with a linear fit to the thermodynamic limit. We find a finite mass gap in the Meissner phase for $J/J_\perp = 2$, $\phi/\pi = 0.2$ and $J/J_\perp = 1.2$, $\phi/\pi = 0.9$ (figures A1(a) and (e)). The mass gap closes in the Meissner phase when lowering $J/J_\perp$. The vortex-liquid phases (figures A1(b) and (d)) and the VL phase (figure A1(c)) have finite mass gaps with weak system-size dependence. The finite mass gap in the vortex-liquid phases confirms that the charge mode does not contribute to the values of the central charges in figures A1(b) and (d) but they are fully accounted for by the two other modes on the three-leg ladder that undergo the commensurate-incommensurate transition.

The analysis of the central charge is more difficult in the regions where the mass gap can not be resolved (or is actually zero) with the system sizes studied in this work. This is the case in the Meissner phase for $J_\perp/J \lesssim 1.6$ and $\phi/\pi \lesssim 0.3$ and in the SC phase (see the inset of figure A1(f)).

Calculating energy gaps is a quite difficult calculation when the gap is small, so where an order parameter exists it is generally better to use it instead to detect the phase boundary of the Mott-insulating region. A suitable order parameter for a Mott phase is the non-local string order parameter [70], given by

$$O_p^2 = \lim_{|j-i|\to\infty} \left\langle \Pi_{r=i}^j (-1)^{1-n_r^t} \right\rangle, \tag{B.2}$$

where $n_r^t = \sum_{\ell=1}^3 n_{r,\ell}$ is the total particle density on rung r.

This can be expressed in terms of a 'kink' operator,

$$p(i) = \Pi_{r<i}(-1)^{1-n_r^t}, \tag{B.3}$$

from which O_p^2 takes the form of a correlation function,

$$O_p^2 = \lim_{|j-i|\to\infty} \langle p(i)p(j) \rangle, \tag{B.4}$$

or, we can construct an extensive order parameter $P = \sum_i p(i)$. We cannot evaluate $\langle P \rangle$ directly, since the sign is indeterminate, however, we can calculate $\langle P^2 \rangle$, which is simply related to O_p^2, as

$$O_p^2 = \langle P^2 \rangle / L^2, \tag{B.5}$$

where L is the length of the lattice. The great advantage of this construction is that the P operator is easy to construct for matrix-product-state algorithms using the triangular matrix-product-operator (MPO) formulation [63, 71], and the expectation value of such triangular MPO's can be evaluated directly in the thermodynamic limit [72]. This allows us to calculate the Binder cumulant [65] of P,

$$B = 1 - \frac{\langle P^4 \rangle}{3\langle P^2 \rangle^2}. \tag{B.6}$$

For an infinite matrix-product-state (iMPS), the expectation value of the nth power of an operator P^n is obtained as a degree n polynomial of the lattice size L, which is exact in the asymptotic large-L limit. Hence the quantity $O_p^2 = \langle P^2 \rangle / L^2$ is evaluated directly as the coefficient of the degree 2 component of $\langle P^2 \rangle$.
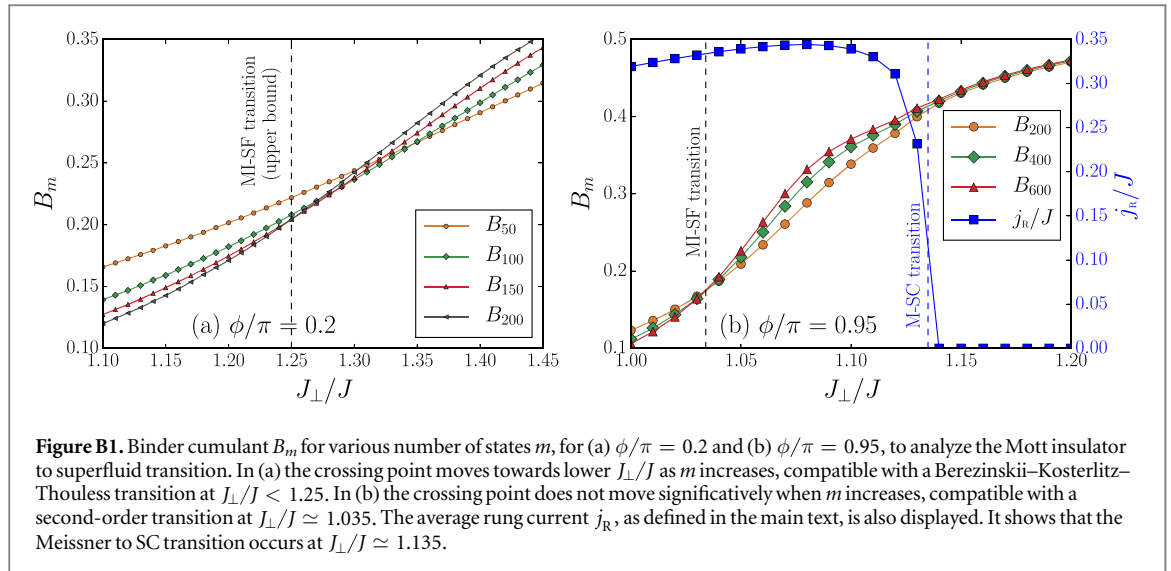
Figure B1. Binder cumulant B_m for various number of states m, for (a) $\phi/\pi = 0.2$ and (b) $\phi/\pi = 0.95$, to analyze the Mott insulator to superfluid transition. In (a) the crossing point moves towards lower $J_\perp/J$ as m increases, compatible with a Berezinskii–Kosterlitz–Thouless transition at $J_\perp/J < 1.25$. In (b) the crossing point does not move significantly when m increases, compatible with a second-order transition at $J_\perp/J \simeq 1.035$. The average rung current j_R, as defined in the main text, is also displayed. It shows that the Meissner to SC transition occurs at $J_\perp/J \simeq 1.135$.

If we evaluate the Binder cumulant directly for an iMPS in the large L limit, then it simply probes where O_p^2 is zero or non-zero, so does not give any additional information. Since the coefficient of the nth degree term in $\langle P^n \rangle$ is simply O_p^n, it follows that if O_p^2 is non-zero then the Binder cumulant in the large L limit is identically equal to $2/3$. Similarly, if $O_p^2 = 0$, then the cumulant expansion of $\langle P^4 \rangle$ reduces to $3 \langle P^2 \rangle^2$ and the Binder cumulant is identically zero. Hence we have a step function located at the point where O_p^2 becomes non-zero, which is what one would expect if one takes the large-L limit of a finite-size Binder cumulant.

However, for an iMPS the correlation length is always finite, so one might expect that finite-entanglement-scaling with the basis size m can be used instead of finite-size scaling. This is indeed the case, if we evaluate the polynomial $\langle P^n \rangle$ at $L = b\xi$, where ξ is the correlation length, and b is some scaling factor. This is equivalent to calculating the order parameter over a finite section of size $L = b\xi$ of the infinite lattice.

Since ξ depends on the number of states m, we can plot a family of curves of the Binder cumulant B_m for different values of m. For a finite system, the value of the Binder cumulant at a second-order critical point is independent of L (up to higher order corrections). For an iMPS, the analogous result is that the critical value of the Binder cumulant is independent of m. Note that for finite size systems the actual value of the Binder cumulant at the critical point is not universal and depends on the boundary conditions [73]. For an iMPS, the value of the m-dependent Binder cumulant depends on the chosen scale factor b. For the calculations here, we use $b = 1$.

As an example, we show in B1 (a) the Binder cumulant as a function of $J_\perp$ for $\phi/\pi = 0.2$. The data is compatible with a Berezinskii–Kosterlitz–Thouless transition from the Meissner Mott-insulating region into the Meissner SF region as $J_\perp/J$ decreases and permits to give an upper bound for the critical point, which is reported in figure 2 in the main text. For $\phi/\pi = 0.95$ (see figure B1(a)), a Mott-insulator to SF transition also occurs in the SC phase and it is compatible with a second-order critical point at $J_\perp/J \simeq 1.035$. The Meissner to SC phase transition, which can be characterized by a rise of the average rung-current j_R, occurs at a distinct point $J_\perp/J \simeq 1.135$.

References

[1] Lin Y J, Compton R L, Jiménez-García K, Porto J V and Spielman I B 2009 *Nature* **462** 628
[2] Dalibard J, Gerbier F, Juzeliūnas G and Öhberg P 2011 *Rev. Mod. Phys.* **83** 1523–43
[3] Lin Y J, Compton R L, Jiménez-García, Phillips W D, Porto J V and Spielman I B 2011 *Nat. Phys.* **7** 531
[4] Aidelsburger M, Atala M, Nascimbène S, Trotzky S, Chen Y A and Bloch I 2011 *Phys. Rev. Lett.* **107** 255301
[5] Jiménez-García K, LeBlanc L J, Williams R A, Beeler M C, Perry A R and Spielman I B 2012 *Phys. Rev. Lett.* **108** 225303
[6] Struck J, Ölschläger C, Weinberg M, Hauke P, Simonet J, Eckardt A, Lewenstein M, Sengstock K and Windpassinger P 2012 *Phys. Rev. Lett.* **108** 225304
[7] Aidelsburger M, Atala M, Lohse M, Barreiro J T, Paredes B and Bloch I 2013 *Phys. Rev. Lett.* **111** 185301
[8] Miyake H, Siviloglou G A, Kennedy C J, Burton W C and Ketterle W 2013 *Phys. Rev. Lett.* **111** 185302
[9] Thouless D J, Kohmoto M, Nightingale M P and den Nijs M 1982 *Phys. Rev. Lett.* **49** 405–8
[10] Hasan M Z and Kane C L 2010 *Rev. Mod. Phys.* **82** 3045–67
[11] Atala M, Aidelsburger M, Barreiro J T, Abanin D, Kitagawa T, Demler E and Bloch I 2013 *Nat. Phys.* **9** 795
[12] Jotzu G, Messer M, Desbuquois R, Lebrat M, Uehlinger T, Greif D and Esslinger T 2014 *Nature* **515** 237–40
[13] Aidelsburger M, Lohse M, Schweizer C, Atala M, Barreiro J T, Nascimbène S, Cooper N R, Bloch I and Goldman N 2015 *Nat. Phys.* **11** 162–66
[14] Carr S T, Narozhny B N and Nersesyan A A 2006 *Phys. Rev. B* **73** 195114

[15] Roux G, Orignac E, White S R and Poilblanc D 2007 *Phys. Rev. B* **76** 195105
[16] Sun G, Jaramillo J, Santos L and Vekua T 2013 *Phys. Rev. B* **88** 165101
[17] Dhar A, Maji M, Mishra T, Pai R V, Mukerjee S and Paramekanti A 2012 *Phys. Rev. A* **85** 041602
[18] Dhar A, Mishra T, Maji M, Pai R V, Mukerjee S and Paramekanti A 2013 *Phys. Rev. B* **87** 174501
[19] Petrescu A and le Hur K 2013 *Phys. Rev. Lett.* **111** 150601
[20] Grusdt F and Höning M 2014 *Phys. Rev. A* **90** 053623
[21] Piraud M, Heidrich-Meisner F, McCulloch I P, Greschner S, Vekua T and Schollwöck U 2015 *Phys. Rev. B* **91** 140406
[22] Greschner S, Piraud M, Heidrich-Meisner F, McCulloch I P, Schollwöck U and Vekua T 2015 arXiv:1504.06564
[23] di Dio M, de Palo S, Orignac E, Citro R and Chiofalo M L 2015 arXiv:1506.03986
[24] Atala M, Aidelsburger M, Lohse M, Barreiro J T, Paredes B and Bloch I 2014 *Nat. Phys.* **10** 588
[25] Mancini M *et al* 2015 arXiv:1502.02495
[26] Stuhl B K, Lu H I, Aycock L M, Genkina D and Spielman I B 2015 arXiv:1502.02496
[27] Harper P G 1955 *Proc. Phys. Soc. A* **68** 879
[28] Hofstadter D R 1976 *Phys. Rev. B* **14** 2239
[29] Jaksch D and Zoller P 2003 *New J. Phys.* **5** 56
[30] Sørensen A, Demler E and Lukin M 2005 *Phys. Rev. Lett.* **94** 086803
[31] Palmer R and Jaksch D 2006 *Phys. Rev. Lett.* **96** 180407
[32] Palmer R, Klein A and Jaksch D 2008 *Phys. Rev. A* **78** 013609
[33] Hafezi M, Sørensen A, Demler E and Lukin M 2007 *Phys. Rev. A* **76** 023613
[34] Möller G and Cooper N 2009 *Phys. Rev. Lett.* **103** 105303
[35] Senthil T and Levin M 2013 *Phys. Rev. Lett.* **110** 046801
[36] Baur S K and Cooper N R 2013 *Phys. Rev. A* **88** 033603
[37] Grusdt F, Letscher F, Hafezi M and Fleischhauer M 2014 *Phys. Rev. Lett.* **113** 155301
[38] Celi A, Massignan P, Ruseckas J, Goldman N, Spielman I B, Juzeliūnas G and Lewenstein M 2014 *Phys. Rev. Lett.* **112** 043001
[39] Zeng T S, Wang C and Zhai H 2015 arXiv:1504.02263
[40] Yan Z, Wan S and Wang Z 2015 arXiv:1504.03223
[41] Ghosh S K, Yadav U K and Shenoy V B 2015 arXiv:1503.02301
[42] Qin F, Wu F, Zhang W, Yi W and Guo G C 2015 *Phys. Rev. A* **92** 023604
[43] Barbarino S, Taddia L, Rossini D, Mazza L and Fazio R 2015 arXiv:1504.00164
[44] Natu S 2015 arXiv:1506.04346
[45] Kardar M 1986 *Phys. Rev. B* **33** 3125–8
[46] Mazo J J, Falo F and Floria L M 1995 *Phys. Rev. B* **52** 10433–40
[47] Trías E, Mazo J J and Orlando T P 2000 *Phys. Rev. Lett.* **84** 741–4
[48] Binder P, Abraimov D, Ustinov A V, Flach S and Zolotaryuk Y 2000 *Phys. Rev. Lett.* **84** 745–8
[49] Dagotto E 1999 *Rep. Prog. Phys.* **62** 1525
[50] Dagotto E and Rice T M 1995 *Science* **271** 618–23
[51] Orignac E and Giamarchi T 2001 *Phys. Rev. B* **64** 144515
[52] Hügel D and Paredes B 2014 *Phys. Rev. A* **89** 023619
[53] Tokuno A and Georges A 2014 *New J. Phys.* **16** 073005
[54] Wei R and Mueller E J 2014 *Phys. Rev. A* **89** 063617
[55] Uchino S and Tokuno A 2015 *Phys. Rev. A* **92** 013625
[56] Petrescu A and le Hur K 2015 *Phys. Rev. B* **91** 054520
[57] White S R 1992 *Phys. Rev. Lett.* **69** 2863
[58] Schollwöck U 2005 *Rev. Mod. Phys.* **77** 259
[59] Schollwöck U 2011 *Ann. Phys., NY* **326** 96
[60] Cabra D C, Honecker A and Pujol P 1997 *Phys. Rev. Lett.* **79** 5126
[61] Cabra D C, Honecker A and Pujol P 1998 *Phys. Rev. B* **58** 6241
[62] White S R 2005 *Phys. Rev. B* **72** 180403
[63] McCulloch I P 2008 arXiv:0804.2509
[64] Crépin F, Laflorencie N, Roux G and Simon P 2011 *Phys. Rev. B* **84** 054517
[65] Binder K 1981 *Z. Phys. B* **43** 119–40
[66] Fölling S, Trotzky S, Cheinet P, Feld M, Saers R, Widera A, Müller T and Bloch I 2007 *Nature* **448** 1029
[67] Vidal G, Latorre J I, Rico E and Kitaev A 2003 *Phys. Rev. Lett.* **90** 227902
[68] Calabrese P and Cardy J 2004 *J. Stat. Mech* **2004** P06002
[69] Eisert J, Cramer M and Plenio M B 2010 *Rev. Mod. Phys.* **82** 277–306
[70] Dalla Torre E G, Berg E and Altman E 2006 *Phys. Rev. Lett.* **97** 260401
[71] McCulloch I P 2007 *J. Stat. Mech.: Theory Exp.* **2007** P10014
[72] Michel L and McCulloch I P 2010 arXiv:1008.4667
[73] Selke W 2006 *Eur. Phys. J. B* **51** 223–8
[74] Ying T, Batrouni G G, Tang G X, Sun X D and Scalettar R T 2014 *Phys. Rev. B* **89** 195128